RSC Advances

PAPER

View Article Online
View Journal | View Issue



Cite this: *RSC Adv.*, 2018, **8**, 11289

# $Sm_2O_3/Co_3O_4$ catalysts prepared by dealloying for low-temperature CO oxidation

Dong Duan, Chunxi Hao, Wenyu Shi, Haiyang Wang and Zhanbo Sun *

Received 8th February 2018
Accepted 7th March 2018

DOI: 10.1039/c8ra01219a

rsc.li/rsc-advances

A series of $Co_3O_4$ catalysts modified by Sm were prepared by a combined dealloying and calcination approach, and the catalytic activities were evaluated using CO catalytic oxidation. The $Sm_2O_3/Co_3O_4$ catalysts were composed of a large number of nanorods and nanosheets, and exhibited a three-dimensional supporting structure with pores. The experimental results revealed that the addition of a small amount of Sm into the precursor AlCo alloy led to a dealloyed sample with improved catalytic activity, and the dealloyed $Al_{90}Co_{9.5}Sm_{0.5}$ ribbons (0.5 $Sm_2O_3/Co_3O_4$) calcined at 300 °C showed the highest activity for CO oxidation with complete CO conversion at 135 °C, moreover, CO conversion almost no attenuation, even after 70 hours of catalytic oxidation, which is superior to that of $Co_3O_4$. The enhanced catalytic activity of the $Sm_2O_3/Co_3O_4$ catalyst can be attributed to the large specific surface area, more reactive oxygen species and $Co^{3+}$ ion, as well as electronic interactions between Sm and Co.



## 1. Introduction

The catalytic oxidation of CO has drawn much attention due to its important applications in industrial catalysis,[1] pollution control,[2,3] gas masks,[4,5] closed-cycle $CO_2$ lasers[6,7] and gas sensors.[8] At present, the mainstream catalyst is a supported catalyst containing noble metal,[9–11] but due to its scarce resources and expensive price, its large-scale industrial application is limited. Increasing the utilization of non-precious metals and the use of non-precious metal catalysts are the two basic ways to save costs. Oxides have become an important direction for the study of low-cost catalysts because of their cheap prices, abundant reserves and unique redox properties.[12]

Transition metal oxides have been widely studied as catalysts for heterogeneous catalysis.[13,14] Among the metal oxides, tricobalt tetraoxide with excellent redox property and rich reserves is the most active for CO oxidation and is a very promising substitute for precious metal catalysts.[15] Xie *et al.*[15] reported that $Co_3O_4$ nanorods not only catalyse CO completely at temperatures as low as −77 °C (the feed gas flow rate was 50 ml $min^{-1}$) but also have high stability in the presence of steam in the feed gas. Song *et al.*[16] reported that the synthesis of mesoporous tricobalt tetroxide by an inverse surfactant micelle method can achieve complete oxidization (100% conversion) of CO to $CO_2$ at −60 °C under normal conditions (~3–10 ppm of $H_2O$ and a flow rate of 20 ml $min^{-1}$) and at 80 °C under moisture rich conditions (~3% $H_2O$ and a flow rate of 20 ml $min^{-1}$).

However, pure $Co_3O_4$ used as a catalyst still has some drawbacks, such as low thermal stability at high temperatures and water deactivation for CO oxidation at low temperatures.[17] In view of this, researches on the modification of $Co_3O_4$-based catalytic materials have drawn much attention. It has been determined that the catalytic performance of $Co_3O_4$ can be significantly improved by doping appropriate rare earth metals as promoters in a $Co_3O_4$ catalyst.[18,19] For example, Hou *et al.*[18] reported that a $CeO_2/Co_3O_4$ catalyst that was prepared by an impregnation method exhibits much better resistance to water vapour poisoning than that of a $Co_3O_4$ catalyst for CO oxidation. Additionally, the $CeO_2/Co_3O_4$ catalyst possesses a higher dispersion degree, smaller particles, and a larger $S_{BET}$, and the interaction between $CeO_2$ and $Co_3O_4$ exists, which may contribute to the excellent water resistance for low-temperature CO oxidation. Liotta *et al.*[19] found that doping a proper amount of $CeO_2$ into the $Co_3O_4$ catalyst significantly improved the catalytic activity and thermal stability due to the presence of $CeO_2$ promoting the efficiency of the $Co^{3+}$–$Co^{2+}$ redox couple.

Lanthanide oxides are well-known effective rare earth catalyst additives. Samarium oxide, one of the lanthanide oxides, has great promise as a good catalyst due to its special properties. Imamura *et al.*[20] reported that the addition of a small amount of Sm (molar ratio Sm/Co = 0.6/10) to $Co_3O_4$ not only enhances its catalytic oxidation activity for toluene but also enhances the thermal stability of $Co_3O_4$. Xu *et al.*[17] studied a series of Sm-modified $Co_3O_4$ catalysts by coprecipitation, and the results show that the addition of a small amount of Sm into $Co_3O_4$ led to an improvement in the catalytic activity for $CH_4$ and CO oxidation. This improvement is due to the addition of a small amount of Sm resulting in the formation of spinel $Co_3O_4$ and amorphous $SmCoO_3$, hence increasing the number of $Co^{3+}$

*School of Science, MOE Key Laboratory for Non-Equilibrium Synthesis and Modulation of Condensed Matter, Key Laboratory of Shaanxi for Advanced Functional Materials and Mesoscopic Physics, Xi'an Jiaotong University, Xi'an 710049, PR China. E-mail: szb@mail.xjtu.edu.cn; Tel: +86 29 82665995*

and the active surface oxygen species, which are responsible for the improvement in the activity. However, only a few studies are reported on preparation of $Sm_2O_3/Co_3O_4$ composites, and the design of $Sm_2O_3/Co_3O_4$ catalyst with high activity is still highly essential and technologically important.

Dealloying is a promising method to prepare various nanoporous materials included noble metals.[21] This method can also be extended to fabricate other oxide composite materials with high catalytic activities.[22] In this work, the $Sm_2O_3/Co_3O_4$ catalyst for CO oxidation was prepared by using dealloying melt-spun Al–Co–Sm alloys in an alkaline solution and calcination in $O_2$. The prepared catalysts exhibited a unique nanorod and nanosheet interconnected structure and showed enhanced catalytic activity for CO oxidation.

## 2. Experiment and method

### 2.1. Preparation

$Al_{90}Co_{10-x}Sm_x$ ($x$ = 0, 0.3, 0.5, 1, 1.5 and 3 at%) and $Al_{90}Sm_{10}$ alloys were prepared from pure Al (99.90 wt%), pure Sm (99.90 wt%) and pure Co (99.99 wt%) by arc-melting using high-purity Ar as the protective atmosphere. The ingot alloys were remelted in a quartz tube on the surface of a single roller with rapid solidification into ribbons at 33 m $s^{-1}$. The as-quenched ribbons were immersed into a 10 wt% NaOH aqueous solution at room temperature for 3 h and then treated at 80 °C for another 10 h to remove residual Al. The acquired samples were repeatedly rinsed with reverse osmosis water and dehydrated alcohol, and dried at 50 °C for 3 h. For simplicity, the samples after dealloying can also be named according to the Sm content in the precursor alloy, that is, $Sm_2O_3$, $Co_3O_4$ and $YSm_2O_3/Co_3O_4$ ($Y$ = 0.3, 0.5, 1, 1.5, and 3). All the dealloyed ribbons were pretreated at 100–500 °C for 2 h in $O_2$ at a total flow rate of 18 ml $min^{-1}$.

### 2.2. Characterization

X-ray diffraction (XRD) patterns of the prepared samples were recorded by a Bruker D8 Advance diffractometer instrument using a Cu Kα target for X-ray irradiation at 20 kV and 40 mA. The microscopic morphology of the samples was observed by field emission scanning electron microscopy (SEM, JSM-7000F microscope) equipped with an INCA X-sight Oxford energy dispersive X-ray spectrometer (EDS) and high-resolution transmission electron microscopy (TEM, JEM-2100 microscope). The nitrogen sorption isotherms, specific surface areas and pore sizes of those prepared samples were measured with a Micromeritics ASAP 2020 apparatus at −77 K. Thermogravimetric analysis (TG) and differential scanning calorimetry (DSC) experiments were carried out on an STA 449C instrument with a heating rate of 10 °C $min^{-1}$. X-ray photoelectron spectroscopy (XPS) was recorded on an Axis Ultra Kratos (UK) multifunctional spectrometer using monochromatic Al Kα radiation (1486.6 eV).

### 2.3. Catalytic evaluation

The catalytic activities of the samples were evaluated using CO catalytic oxidation. One-hundred milligrams of the catalyst was placed into a quartz tube with an inner diameter of 6 mm for the measurements, and an asbestos column with a length of approximately 1 cm was used to fix the catalyst. Then, the quartz tube was placed into a variable temperature reaction furnace. A reaction gas mixture consisting of 1% CO, 10% $O_2$ and 89% $N_2$ (volume) was fed into the reactor using a mass flow metre (Brooks 5850E) at a total flow rate of 100 ml $min^{-1}$ (60 000 $h^{-1}$). The concentration of produced $CO_2$ and unreacted CO gas was analysed online with a GC-7900 gas chromatograph equipped with a flame ionization detector (FID). The CO conversion rate (%) was determined by the changes in the inlet and outlet CO concentration with the following formula:

$$CO_{conversion} = \frac{C_{in} - C_{out}}{C_{in}} \times 100\%$$

where $C_{in}$ represents the inlet CO concentration and $C_{out}$ is the outlet CO concentration.

## 3. Results and discussion

### 3.1. Phase constituents and microstructure of the dealloyed samples

Fig. 1 shows the XRD patterns and EDS results of the dealloyed samples calcined at different temperatures. Only the definite diffraction peaks of $Co_3O_4$ appear in the diffraction pattern after the $Al_{90}Co_{9.5}Sm_{0.5}$ samples were dealloyed and calcined at 300 °C. After the samples were annealed at 700 °C or 800 °C, the diffraction peak of $Sm_2O_3$ still was not apparent (Fig. 1(a)). However, as shown in Fig. 1(b), the atomic ratio of Sm to Co is close to the mean composition in the precursor, indicating that the loss of Sm and Co was small during the dealloying, and the peaks cannot be detected by XRD due to the low Sm content. The residual Al contents were less than 3.93 at% (Fig. 1(b)) of the dealloyed samples obtained from the $Al_{90}Co_{9.5}Sm_{0.5}$ alloys. At the same time, note that when the content of Sm is increased to 30%, a weak diffraction peak of $Sm_2O_3$ appears, and the diffraction peak of $Co_3O_4$ disappears, indicating that the addition of rare earth Sm may suppress the crystallization of $Co_3O_4$, which is similar to that of the oxide $CeO_2$.[12]

The SEM images of dealloyed $Al_{90}Co_{10}$, $Al_{90}Sm_{10}$ and $Al_{90}Co_{9.5}Sm_{0.5}$ ribbons calcined at 300 °C are shown in Fig. 2. For $Sm_2O_3$ and $Co_3O_4$, the samples exhibit a nanosheet and

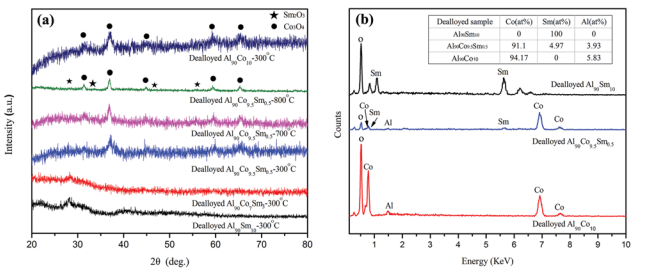


Fig. 1 (a) XRD patterns of the dealloyed $Al_{90}Co_{10}$, $Al_{90}Sm_{10}$, $Al_{90}Co_7Sm_3$ ribbons calcined at 300 °C and $Al_{90}Co_{9.5}Sm_{0.5}$ ribbons calcined at 300, 700 and 800 °C. (b) EDS patterns of the dealloyed $Al_{90}Co_{10}$, $Al_{90}Sm_{10}$ and $Al_{90}Co_{9.5}Sm_{0.5}$ ribbons calcined at 300 °C.

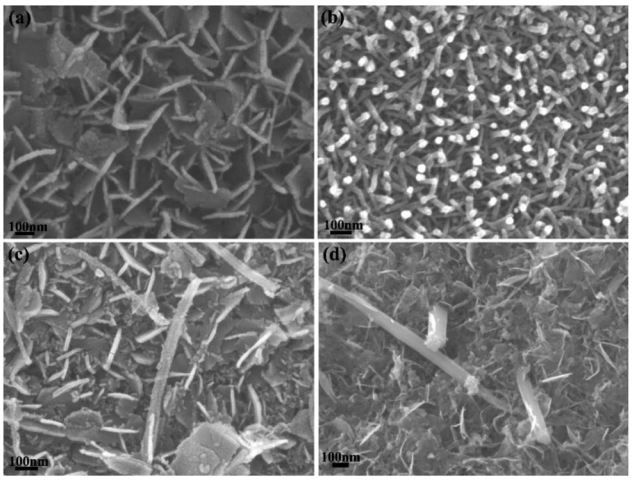


Fig. 2 SEM images of dealloyed $Al_{90}Co_{10}$ (a), $Al_{90}Sm_{10}$ (b) and $Al_{90}Co_{9.5}Sm_{0.5}$ (c); and (d) calcined at 300 °C.

nanorod morphologies, respectively. The nanosheet thickness is approximately 30 nm, and the nanorod diameter is approximately 20–30 nm with excellent uniformity, which can be seen in Fig. 2(a) and (b). However, the plan-view image exhibited a unique nanorod and nanosheet interconnected structure for the $Sm_2O_3/Co_3O_4$ prepared from the dealloyed $Al_{90}Co_{9.5}Sm_{0.5}$ ribbons calcined at 300 °C, see Fig. 2(c), and the cross-sectional image exhibited a three-dimensional porous ligament structure composed of many nanosheets and nanorods interpenetrated with each other, see Fig. 2(d).

The TEM images and corresponding selected-area electron diffraction patterns of dealloyed $Al_{90}Co_{9.5}Sm_{0.5}$ ribbons calcined at 300 °C are presented in Fig. 3. The sample is composed of nanorods and nanosheets, consistent with the SEM results, and the nanosheets contain many micropores, as shown in Fig. 3(a). The diffraction rings of the SAED pattern (Fig. 3(b)) were indexed to $Co_3O_4$ (440), (511), and (220) and $Sm_2O_3$ (400), (440), and (211), which verified the coexistence of $Co_3O_4$ and $Sm_2O_3$. Fig. 3(c) and (d) shows the HRTEM images of the nanorods and nanosheets in Fig. 3(a). The lattice spacing in Fig. 3(c) is approximately 0.286 nm, which corresponds to the (220) plane of $Co_3O_4$. The lattice spacings in Fig. 3(d) are approximately 0.269 nm and 0.193 nm, which correspond to the (400) and (440) planes of $Sm_2O_3$, respectively. According to these results, $Sm_2O_3$ is present in the form of nanorods, and $Co_3O_4$ is present in the form of nanosheets in the sample of dealloyed $Al_{90}Co_{9.5}Sm_{0.5}$ ribbons. When calcined at 300 °C, the $Sm_2O_3$ nanorods and $Co_3O_4$ nanosheets stacked together constitute a rough interface, and the interface interaction is significantly enhanced between them.

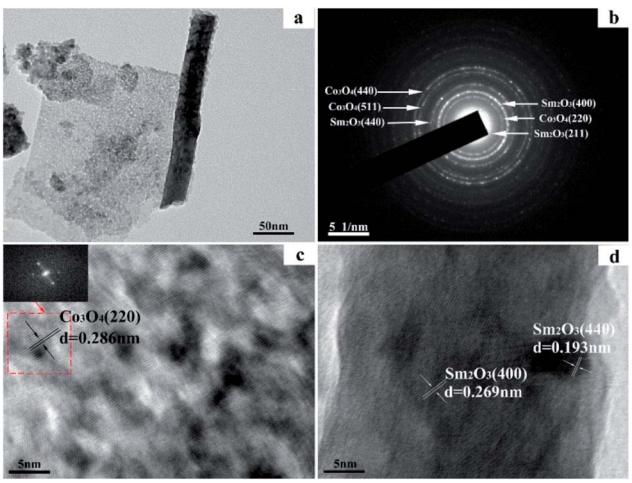


Fig. 3 TEM image (a), corresponding selected-area electron diffraction pattern (b) and HRTEM images (c) and (d) of the dealloyed $Al_{90}Co_{9.5}Sm_{0.5}$ ribbons calcined at 300 °C.

### 3.2. Physical and surface properties

Fig. 4 shows the $N_2$ adsorption–desorption isotherms and the corresponding pore size distribution curves for the dealloyed $Al_{90}Co_{10}$, $Al_{90}Sm_{10}$ and $Al_{90}Co_{9.5}Sm_{0.5}$ ribbons calcined at 300 °C. The $N_2$ sorption isotherms of all the samples were type IV with hysteresis loops, indicative of their mesoporous structures. The BET surface area ($S_{BET}$), pore size ($D_P$) and pore volume ($V_P$) of these samples are listed in Table 1. As seen from Table 1, the BET surface area and pore volume of all the $Sm_2O_3/Co_3O_4$ composites are larger than those of the $Co_3O_4$ and $Sm_2O_3$, and the 0.5 $Sm_2O_3/Co_3O_4$ composite has the largest specific surface area, 95.72 $m^2\ g^{-1}$, which is approximately three times of that of $Sm_2O_3$ and $Co_3O_4$. The results show that the addition of the $Sm_2O_3$ nanorods can effectively refine the porous structure. Fig. 4(b) is the corresponding pore size distribution curve for the three catalysts. Compared to $Sm_2O_3$ and $Co_3O_4$, the 0.5 $Sm_2O_3/Co_3O_4$ composite has a narrower pore size distribution and a smaller pore size with an average pore size of approximately 8.355 nm. This structure is a typical porous structure, which is suitable for CO catalytic oxidation.

Fig. 5 shows the TGA–DSC curves for the dealloyed $Al_{90}Co_{9.5}Sm_{0.5}$ ribbons in $O_2$/Ar atmosphere. The sample has mainly three weight loss stages. The first stage exhibits a 10.01% weight loss below 250 °C, which is attributed to the removal of physically adsorbed $H_2O$. Note that there is a pronounced exothermic peak at 213 °C due to the oxidation of Co and the crystallization of $Co_3O_4$.[17] In the temperature range of 250–950 °C, corresponding to the slow crystallization process of $Co_3O_4$ and $Sm_2O_3$ formed, the TG curve weight decreased by approximately

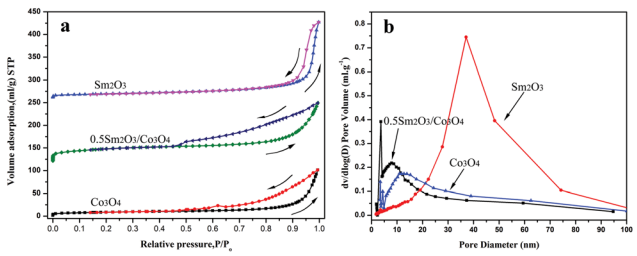


Fig. 4 $N_2$ adsorption–desorption isotherms and corresponding pore size distribution curves at 77 K of the dealloyed $Al_{90}Co_{10}$, $Al_{90}Sm_{10}$ and $Al_{90}Co_{9.5}Sm_{0.5}$ ribbons calcined at 300 °C.

Table 1 The BET surface area ($S_{BET}$), average pore diameter ($D_p$) and pore volume ($V_p$) of the dealloyed $Al_{90}Co_{10-x}Sm_x$ ($x$ = 0, 0.3, 0.5, 1, 1.5 and 3 at%) and $Al_{90}Sm_{10}$ alloys calcined at 300 °C

| Sample | $S_{BET}$/m$^2$ g$^{-1}$ | $D_p$/nm | $V_p$/cm$^3$ g$^{-1}$ |
|---|---|---|---|
| $Co_3O_4$ | 30.38 | 20.628 | 0.157 |
| 0.3 $Sm_2O_3/Co_3O_4$ | 58.34 | 11.442 | 0.168 |
| 0.5 $Sm_2O_3/Co_3O_4$ | 95.72 | 8.355 | 0.200 |
| 1 $Sm_2O_3/Co_3O_4$ | 86.82 | 11.140 | 0.242 |
| 1.5 $Sm_2O_3/Co_3O_4$ | 55.62 | 16.350 | 0.227 |
| 3 $Sm_2O_3/Co_3O_4$ | 41.55 | 22.148 | 0.230 |
| $Sm_2O_3$ | 33.68 | 30.672 | 0.258 |

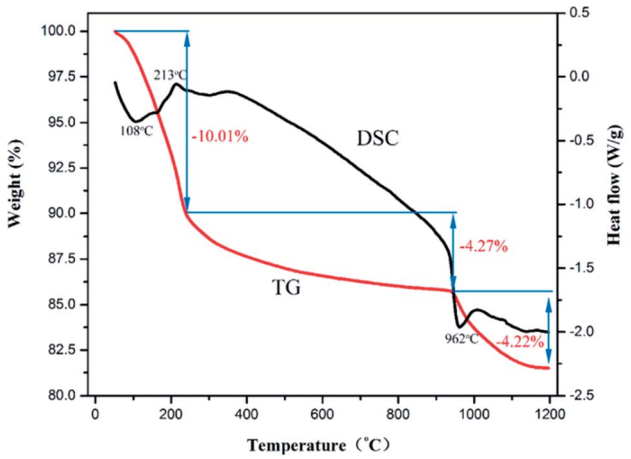


Fig. 5 TGA–DSC curves for the dealloyed $Al_{90}Co_{9.5}Sm_{0.5}$ ribbons in $O_2$/Ar atmosphere.

4.27%. At 962 °C, there is a distinct endothermic peak, which corresponds to a sharp decrease of approximately 4.22% in the TG curve due to the decomposition of $Co_3O_4$ into CoO and $O_2$, and the corresponding equation is $2Co_3O_4 = 6CoO + O_2\uparrow$.[17,38]

Fig. 6 shows the O 1s, Sm 3d and Co 2p XPS spectra of the $Sm_2O_3$ nanorod, 0.5 $Sm_2O_3/Co_3O_4$ composite and $Co_3O_4$ nanosheet. The O 1s spectrum of the $Sm_2O_3/Co_3O_4$ composite consisted of three peaks. The peaks centred at ~529.95 eV ($O_{lat}$), ~531.3 eV ($O_{sur}$), and ~532.9 eV ($O_{H_2O}$) were assigned to lattice oxygen species, surface adsorbed and weakly bonded oxygen species, and adsorbed water, respectively, according to ref. 23 and 24. It is generally accepted that surface oxygen species are usually active oxygen species for catalytic reactions, which could be explained using the relative quantity of $O_{sur}$ species, *i.e.*, 31.27% and 47.79% for $Co_3O_4$ and $Sm_2O_3/Co_3O_4$, respectively. The results show that there were more active oxygen species existed on the surface of the $Sm_2O_3/Co_3O_4$ composite compared with $Co_3O_4$.

Fig. 6(b) presents Sm 3d XPS spectra that is deconvolved into two peaks. According to the literature,[25] the low-energy peak (Sm $3d_{5/2}$) at 1083.5 eV and the high-energy peak (Sm $3d_{3/2}$) at 1110.6 eV were attributed to $Sm^{3+}$ ($Sm_2O_3$), according to the literature.[25] Note that the Sm 3d spectra of the $Sm_2O_3/Co_3O_4$ composite shifts nearly 0.6 eV compared to $Sm_2O_3$, indicating

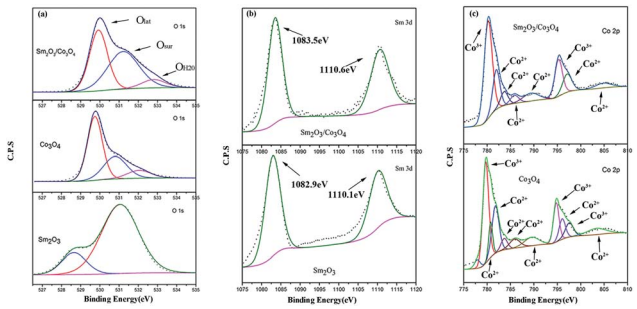


Fig. 6 XPS spectra of $Sm_2O_3$, $Co_3O_4$ and $Sm_2O_3/Co_3O_4$ for the O 1s peaks (a), Sm 3d peaks (b) and Co 2p peaks (c).

that there is an electronic interaction between Sm and Co. The XPS pattern of Co 2p is shown in Fig. 6(c). For the $Sm_2O_3/Co_3O_4$ composite, the peaks at 780.2 eV and 795.25 eV are assigned to $Co^{3+}$ and the other six peaks (781.95 eV; 797.1 eV; 783.65 eV; 785.85 eV; 789.35 eV; and 804.80 eV) represent the presence of $Co^{2+}$.[26–31] According to the literature,[15,17] $Co^{3+}$ was responsible for the improvement in the activity, and the concentration of $Co^{3+}$ ions can be expressed using the ratio of their corresponding spectral areas to the total area ($Co^{2+}$ + $Co^{3+}$). The ratios were 56.5% for $Sm_2O_3/Co_3O_4$ and only 46.6% for $Co_3O_4$, indicating that there were more $Co^{3+}$ ions on the surface in the $Sm_2O_3/Co_3O_4$ catalyst. Therefore, the introduction of $Sm_2O_3$ to the $Co_3O_4$ resulted in an increase in $Co^{3+}$ species and active oxygen species that facilitates an electronic interaction between Sm and Co, which improves the redox potential of the $Co_3O_4$-based catalysts.

### 3.3. CO catalytic oxidation

Fig. 7(a) shows the catalytic performance of the $Sm_2O_3$, $Co_3O_4$ and $Sm_2O_3/Co_3O_4$ catalysts with different $Sm_2O_3$ contents for the CO catalytic oxidation. The results show that the catalytic activity of all the $Sm_2O_3/Co_3O_4$ catalysts were greater than that of $Sm_2O_3$ and $Co_3O_4$. The CO conversion increased progressively as the content of Sm increased up to 0.5 at% in the precursory alloy, and then decreased with a Sm content above 0.5 at%. The CO conversion over $Sm_2O_3/Co_3O_4$ from the $Al_{90}Co_{9.5}Sm_{0.5}$ alloy was more than 99% at 135 °C, while the conversions of $Co_3O_4$ and $Sm_2O_3$ were only approximately 35%

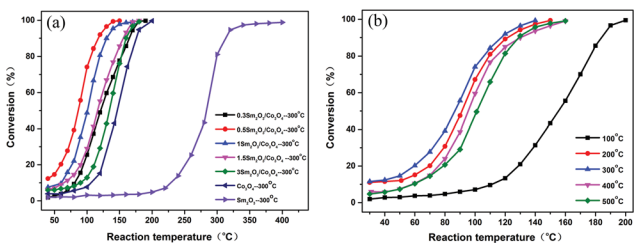


Fig. 7 CO conversion as a function of reaction temperature over the $Sm_2O_3$, $Co_3O_4$ and $Sm_2O_3/Co_3O_4$ catalysts with different $Sm_2O_3$ contents (a) and the 0.5 $Sm_2O_3/Co_3O_4$ catalyst calcined at different temperatures (b).

and 3%, respectively. The temperature at which the conversion was 50% ($T_{50}$) for $Sm_2O_3/Co_3O_4$ from the $Al_{90}Co_{9.5}Sm_{0.5}$ alloys was 85 °C, which was much lower than that of $Co_3O_4$ (147 °C) and $Sm_2O_3$ (285 °C). These results indicated that the $Sm_2O_3/Co_3O_4$ catalyst from the $Al_{90}Co_{9.5}Sm_{0.5}$ alloys exhibited an excellent ability to oxidize CO compared with the pure metal oxide counterparts.

The CO conversion plots as a function of reaction temperature over the 0.5 $Sm_2O_3/Co_3O_4$ catalyst calcined at different temperatures are shown in Fig. 7(b). The catalytic activity was significantly enhanced when the sample was calcined above 200 °C. For the 0.5 $Sm_2O_3/Co_3O_4$ samples calcinated at different temperatures, the order of catalytic activity is obtained as follows: calcined at 100 °C < calcined at 500 °C < calcined at 400 °C < calcined at 200 °C < calcined at 300 °C. The experimental results indicated that the calcination temperature has an important influence on the catalytic activity of the sample.

The long-term stability of the $Co_3O_4$ and 0.5 $Sm_2O_3/Co_3O_4$ catalysts were evaluated and the results is are in Fig. 8(a). The $Sm_2O_3/Co_3O_4$ catalyst exhibited near 100% CO conversion without a noticeable deterioration in activity, even at high reaction rate, CO conversion only decays from 37% to 33%. However, CO conversion of the $Co_3O_4$ catalyst decreased from 37% to 23% when the holding time was 70 h at 140 °C. This result implied that the addition of $Sm_2O_3$ is conducive to maintaining a high stability.

Fig. 8(b) shows the effect of the oxygen concentration on the CO conversion over the 0.5 $Sm_2O_3/Co_3O_4$ catalyst calcined at a 300–140 °C constant temperature. As for the catalyst, the CO/$O_2$ ratio has an important effect on the catalytic activity for CO oxidation. The effects of changing from $O_2$-rich (10% $O_2$), CO-rich (0–0.5% $O_2$) to a close-to-stoichiometric (1% $O_2$) and $O_2$-rich gas mixtures were investigated. The catalyst was tested directly with the reactant gas (1% CO/10% $O_2$/89% $N_2$) at 140 °C for 50 min. As the $O_2$ concentration decreased from 10% to 0%, as the residual $O_2$ continued to be consumed, the CO conversion decreased sharply from 99% to 12%, then tended to be steady. The reason for the phenomenon maybe is caused by the surface lattice oxygen of catalyst reacted with CO and conforms to the Mars–van Krevelen type mechanism. When $O_2$ concentration increased to 0.3%, the CO conversion increased abruptly from 12% to 76%, according to equation $2CO + O_2 = 2CO_2$. The complete reaction cannot be achieved because 0.3% of $O_2$ can only react with 0.6% of CO. As the oxygen content continued to increase to an $O_2$-rich condition, the final CO conversion reached the initial 99%. During the increase in the $O_2$ concentration from 0.5% to 10%, a new steady-state can be rapidly rebuilt. These results show that during CO oxidation, the activity is strongly affected by the reactant gas mixture composition. Above results clearly indicated that the prepared $Sm_2O_3/Co_3O_4$ catalyst can exhibit enhanced catalytic activity and higher catalytic stability without a deactivation in activity after an extended time test.

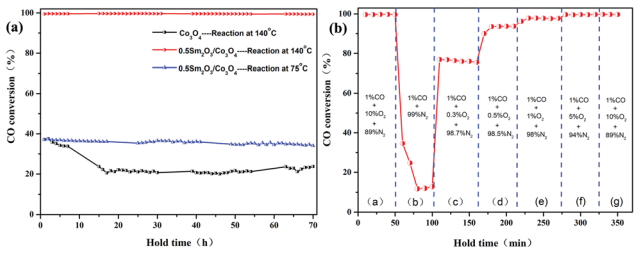


Fig. 8 Long-term stability of the $Co_3O_4$ and 0.5 $Sm_2O_3/Co_3O_4$ catalysts for 70 h (reaction conditions: 1% CO, 10% $O_2$ and 89% $N_2$) (a) and the catalytic performance of 0.5 $Sm_2O_3/Co_3O_4$ catalysts under different oxygen concentrations at 140 °C (flow rate: 100 ml $min^{-1}$) (b).

### 3.4. Analysis and discussion

In the present work, the $Sm_2O_3/Co_3O_4$ catalyst with a high catalytic activity was obtained using a facile chemical dealloying and calcination method. During the dealloying process, melt-spun Al–Co–Sm alloys can preserve the structure and monolithic characteristics of the parent alloy at a macroscale because diffusion only occurs in the domain size.[21] When the melt-spun Al–Co–Sm alloys were immersed in a NaOH solution, the Al atoms were progressively removed, and the Co atoms and Sm atoms on the surface were exposed to the alkaline solution. These lower coordinated metal atoms are highly active,[32] which were likely to combine with $OH^-$ ions from $H_2O$ to form hydroxide at 80 °C. During this process, $Sm(OH)_3$ can form nanorods due to the anisotropic growth of different nuclei under the basic hydrothermal condition, and $Co(OH)_3$ aggregates and grows into nanosheet structures. $Co(OH)_3$ and $Sm(OH)_3$ could easily transform into $Co_3O_4$ and $Sm_2O_3$ by dehydration during calcination in $O_2$, and due to the calcination, the nanorods and nanosheets are closely interconnected, forming a rough interface and enhancing the synergistic effect between the $Sm_2O_3$ and $Co_3O_4$. In addition to its inherent simplicity, the dealloying method can effectively avoid surface contamination of the preparative nanomaterials by organic chemicals or other surface-directing molecules, which is often seen in wet chemical synthesis at elevated temperatures.[33]Thus, this preparation method is a promising strategy for large-scale production.

The BET and XPS analyses suggested that the introduction of trace $Sm_2O_3$ greatly enhanced the specific surface area of the catalyst, and created more active oxygen species and $Co^{3+}$ ions, according to the literature.[15] Additionally, the more $Co^{3+}$ ions are created, the more active catalytic sites exist. On the other hand, the $Sm_2O_3$ nanorods and $Co_3O_4$ nanosheets are tightly connected to create many nanoscale interfaces, where the generated free electrons can easily migrate at the interfaces[37] (Fig. 6(b)). These electrons not only transform molecular oxygen into an active oxygen species to interact with CO molecules adsorbed at the interfaces but also weaken the $CO_2$ bond and accelerate $CO_2$ dissociation, leading to an increase in the reaction rate.[12] In addition, the $Sm_2O_3/Co_3O_4$ catalyst possessed a higher specific surface area (95.72 $m^2\ g^{-1}$), narrower pore size distribution and more uniform pores than those of $Co_3O_4$ and $Sm_2O_3$ (Fig. 4), which also enlarged the contact interface accessibility or adsorbing molecules. All of these factors play a very positive role in the catalytic oxidation of CO.

Experimental and theoretical studies have widely discussed the CO oxidation reaction mechanism. Behm *et al.*[34] showed

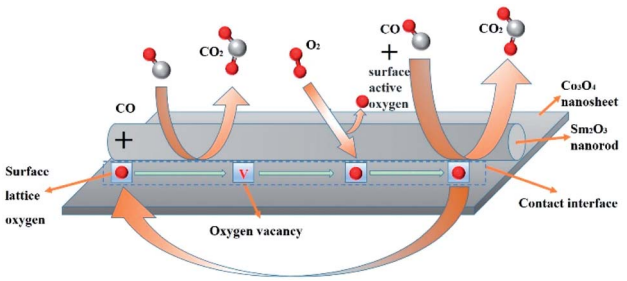


Fig. 9 Possible CO oxidation reaction pathway on $Sm_2O_3/Co_3O_4$ catalyst.

that surface lattice oxygen is the active oxygen species for the CO oxidation, which follows an Au-assisted Mars–van Krevelen mechanism. Zhang *et al.*[35] showed that the molecularly oxygen absorbed on both surface vacancies and lattice oxygen should participate in the CO oxidation. Zhang *et al.*[36] reported that both oxygen on PTA (phosphotungstic acid) and oxygen molecules in the reaction gas are involved in the CO catalytic oxidation reaction. A possible CO oxidation reaction pathway on $Sm_2O_3/Co_3O_4$ catalyst is proposed in Fig. 9, by piecing together information from different techniques. Firstly, the surface lattice oxygen reacts with adsorbed CO and generates oxygen vacancies, and then reconnects with the molecular oxygen in the reaction gas, part of the molecular oxygen replenishes the missing surface lattice oxygen, and the other part adsorbed on the surface of the catalyst becomes the surface active oxygen, which directly reacts with CO, so the catalytic oxidation of CO can be long-term and stable.

## 4. Conclusions

We have developed a simple and effective method for fabricating a $Sm_2O_3/Co_3O_4$ catalyst by means of dealloying in a 10 wt% NaOH aqueous solution and calcination in $O_2$. Our results indicated that the $Sm_2O_3/Co_3O_4$ catalyst exhibits excellent catalytic activity for CO oxidation at ambient temperature. The enhanced catalytic activity of the $Sm_2O_3/Co_3O_4$ catalyst can be attributed to the large specific surface area, more reactive oxygen species and $Co^{3+}$ ions, and electronic interactions between Sm and Co. In addition, the $Sm_2O_3/Co_3O_4$ catalyst showed good long-term catalytic stability and even after 70 hours, CO conversion still almost no attenuation. It is expected that many other useful metal oxide composites can be fabricated in a similar manner.

## Conflicts of interest

There are no conflicts to declare.

## Acknowledgements

This work was supported by the National Natural Science Foundation of China (Grant No. 51771141 and 51371135 and 51671155).

## Notes and references

1 A. Mart Nez-Arias, M. Fernández-Garc A, O. Gálvez, J. M. Coronado, J. A. Anderson, J. C. Conesa, J. Soria and G. Munuera, *J. Catal.*, 2000, **195**, 207–216.
2 S. Jirawongnuson, W. Wachirapan, T. Suthiprasert and E. Wirojsakunchai, *Key Eng. Mater.*, 2015, **656–657**, 538–543.
3 T. Suthiprasert, T. Limpurimongkol, S. Jirawongnuson, T. Aroonsrisopon and E. Wirojsakunchai, *Eng. J.*, 2017, **21**, 93–103.
4 D. K. Kim, B. I. Kim, C. H. Shin and C. S. Shin, *Journal of the Korean Society of Safety*, 2006, 35–45.
5 H. S. Kong and S. H. Kim, *Int. J. Pharm. Technol.*, 2016, **8**, 26870–26875.
6 D. R. Schryer, B. T. Upchurch, R. V. Hess, G. M. Wood, B. D. Sidney, I. M. Miller, K. G. Brown, J. D. Vannorman, J. Schryer and D. R. Brown, Low-Temperature CO-Oxidation Catalysts for Long-Life $CO_2$ Lasers, *NASA Conf. Publ.*, 1990, **1**, 41–53.
7 A. V. Bondarenko, V. D. Gavrilyuk, V. S. Golubev, F. V. Lebedev and M. M. Smakotin, *Quantum Electron.*, 1980, **10**, 775–780.
8 N. Barsan and U. Weimar, *J. Phys.: Condens. Matter*, 2003, **15**, R813.
9 S. A. Nikolaev, E. V. Golubina, I. N. Krotova, M. I. Shilina, A. V. Chistyakov and V. V. Kriventsov, *Appl. Catal., B*, 2015, **168–169**, 303–312.
10 A. Luengnaruemitchai, K. Srihamat, C. Pojanavaraphan and R. Wanchanthuek, *Int. J. Hydrogen Energy*, 2015, **40**, 13443–13455.
11 H. Zhu, Z. Qin, W. Shan, W. Shen and J. Wang, *J. Catal.*, 2004, **225**, 267–277.
12 X. Zhang, K. Li, W. Shi, C. Wei, X. Song, S. Yang and Z. Sun, *Nanotechnology*, 2017, **28**, 045602.
13 C. Stampfl and M. Scheffler, *Surf. Sci.*, 1999, **433–435**, 119–126.
14 J. Jansson and C. T. H. Gskola, Chalmers University of Technology, 2002.
15 X. Xie, Y. Li, Z. Q. Liu, M. Haruta and W. Shen, *Nature*, 2009, **458**, 746.
16 W. Song, A. S. Poyraz, Y. Meng, Z. Ren, S. Y. Chen and S. L. Suib, *Chem. Mater.*, 2012.
17 X. Xu, H. Han, J. Liu, W. Liu, W. Li and X. Wang, *J. Rare Earths*, 2014, **32**, 159–169.
18 X. D. Hou, Y. Z. Wang and Y. X. Zhao, *Catal. Lett.*, 2008, **123**, 321–326.
19 L. F. Liotta, G. D. Carlo, G. Pantaleo, A. M. Venezia and G. Deganello, *Appl. Catal., B*, 2006, **66**, 217–227.
20 S. Imamura, K. Fukuda, T. Nishida and T. Inui, *J. Catal.*, 1985, **93**, 186–191.
21 I. Mccue, E. Benn, B. Gaskey and J. Erlebacher, *Annu. Rev. Mater. Res.*, 2016, **46**, 263–286.
22 X. Zhang, G. Li, S. Yang, X. Song and Z. Sun, *Microporous Mesoporous Mater.*, 2016, **226**, 61–70.
23 N. S. Mcintyre, D. D. Johnston, L. L. Coatsworth, R. D. Davidson and J. R. Brown, *Surf. Interface Anal.*, 1990, **15**, 265–272.

24 L. Armelao, D. Barreca, S. Gross and E. Tondello, *Surf. Sci. Spectra*, 2001, **8**, 14–23.
25 N. Sasmal, M. Garai and B. Karmakar, *Journal of Asian Ceramic Societies*, 2016, **4**, 29–38.
26 C. A. Strydom and H. J. Strydom, *ChemInform*, 1989, **20**, 191–195.
27 J. P. Bonnelle, J. Grimblot and A. D'Huysser, *J. Electron Spectrosc. Relat. Phenom.*, 1975, **7**, 151–162.
28 C. V. Schenck, J. G. Dillard and J. W. Murray, *J. Colloid Interface Sci.*, 1983, **95**, 398–409.
29 J. C. Carver, G. K. Schweitzer and T. A. Carlson, *J. Chem. Phys.*, 1972, **57**, 973–982.
30 B. J. Tan, K. J. Klabunde and P. M. A. Sherwood, *J. Am. Chem. Soc.*, 1991, **113**, 855–861.
31 G. Mattogno, C. Ferragina, M. A. Massucci, P. Patrono and A. L. Ginestra, *J. Electron Spectrosc. Relat. Phenom.*, 1988, **46**, 285–295.
32 C. Xu, Y. Liu, C. Zhou, L. Wang, P. H. Geng and P. Y. Ding, *Chemcatchem*, 2011, **3**, 399–407.
33 B. Varghese, C. H. Teo, Y. Zhu, M. V. Reddy, B. V. R. Chowdari, A. T. S. Wee, V. B. C. Tan, C. T. Lim and C. H. Sow, *Adv. Funct. Mater.*, 2007, **17**, 1932–1939.
34 D. Widmann and R. J. Behm, *Acc. Chem. Res.*, 2014, **47**, 740–749.
35 X. Zhang, D. Duan, G. Li, W. Feng, S. Yang and Z. Sun, *Nanotechnology*, 2018, **29**(9), 095606.
36 B. Zhang, H. Asakura and N. Yan, *Ind. Eng. Chem. Res.*, 2017, **56**, 3578–3587.
37 Z. Zhang, Y. Zhu, H. Asakura, B. Zhang, J. Zhang, M. Zhou, Y. Han, T. Tanaka, A. Wang and T. Zhang, *Nat. Commun.*, 2017, **8**, 16100.
38 T. Zhang, P. Hing, H. Huang and J. Kilner, *J. Eur. Ceram. Soc.*, 2002, **22**, 27–34.